Journal of Building Technology, 2024, Volume 6, Issue 2
DOI: 10.32629/jbt.v6i2.2547
ISSN Online: 2717-5103
ISSN Print: 2705-1390

Reinforcement of Concrete Structures with High-Performance Fiber-reinforced Concrete (HPFRC)

Frediani Matías, Almenar Martín, Luccioni Bibiana

Institute of Structures, School of Exact Sciences and Technology, National University of Tucuman, La Rioja, Argentina.

Abstract: The incorporation of high quality fibers into very high strength concrete matrices leads to materials that are especially suitable to withstand extreme loads. For this reason, these materials are adequate for reinforcement and durability improvement of buildings and infrastructure constructions. The general objective of this work is to numerically study the flexural behavior of concrete structural elements reinforced with HPFRC. This general goal includes the analysis of the effect of the different variables, the content and type of fibers, as well as the thickness of the reinforcement. The results of this analysis can contribute to improving the efficiency of the intervention techniques. For this purpose, numerical models are calibrated to reproduce the behavior observed in experimental tests carried out on HPFRC elements. Then the models are used to reproduce reinforced concrete beams reinforced with HPFRC under flexural loading. Finally, the effect of the aforementioned design variables on the behavior of reinforced beams is studied using the calibrated models. The results show the efficiency of the intervention increases with the fiber content and thickness of the reinforcement layer. However, the definition of the optimal design should also consider other criteria, such as constructional limitations and cost analysis.

Key words: HPFRC; reinforcement; concrete beams; numerical models

1. Introduction

Civil constructions constitute a significant percentage of a country's capital. Both maintenance and reconstruction imply the availability of important resources that, undoubtedly, must be optimized. HPFRCs incorporate high-quality fibers in very high-strength matrices (> 100 MPa) to obtain materials that are especially suitable for withstanding extreme actions, making them promising materials for reinforcing and improving the durability of buildings and various infrastructure works.

The reinforcement of reinforced concrete structures with HPFRC has some advantages over other systems, such as greater resistance to high temperatures and ultraviolet radiation, and greater compatibility with the concrete of the structure to be reinforced, which prevents brittle failure of the interface (Nanni, 2012). Although existing results show the potential applications of HPFRC as a reinforcement layer, further research is required to understand its behavior under extreme loads. The combination of high performance with high economic efficiency is still elusive (Tysmans et al., 2015). The general objective of this work is to contribute to the development of the design and application of HPFRC for a better exploitation of the advantages and alternatives of these materials for reinforcement of reinforced concrete structures. The particular

objective is the numerical reproduction of the behavior of reinforced concrete elements reinforced with HPFRC subjected to bending and comparison with experimental results.

Fiber composites can be simulated with models formulated at different scales. In macro-models, the composite behavior is represented by an equivalent homogeneous material model with average properties. This type of model is typically used in phenomenological approaches where the constitutive laws are derived from laboratory tests (Yu et al., 2015). In this work, the numerical simulations were performed by the Ansys Workbench program, using a macro model available in its library.

2. Constitutive Model Used

An elastoplastic model was used to reproduce the behavior of the concrete. In this model, the relationship between the stress tensor σ, the strain tensor ε and the plastic strain tensor ε^{pl} is given by:

$$\boldsymbol{\sigma} = \boldsymbol{C}\,(\boldsymbol{\varepsilon} - \boldsymbol{\varepsilon}^{\boldsymbol{pl}}) \quad (1)$$

Where, *C* is the fourth order elastic constitutive tensor for a linear and isotropic elastic material. This tensor is determined by the elastic parameters *E* and μ, which are Young's modulus and Poisson's ratio, respectively. The increment of the plastic deformations is calculated by the following flow rule:

$$\dot{\boldsymbol{\varepsilon}}^{\boldsymbol{pl}} = \dot{\lambda}\,\frac{\partial Q_{MW}}{\partial \boldsymbol{\sigma}} \quad (2)$$

where Q_{MW} is a function of the potential to be defined later and λ is the increment of the plastic multiplier. The plastic multiplier can be determined by means of the loading and unloading conditions defined below:

$$f_{MW} \leq 0, \quad \dot{\lambda} \geq 0, \quad f_{MW}\,\dot{\lambda} = 0 \quad (3)$$

Where f_{MW} is the yield surface. This model uses the creep surface of Menetrey and Willam (1995), which is schematized in Fig. 1. Within this surface, the material exhibits an isotropic linear elastic behavior. However, when the material reaches a certain stress threshold on this surface, it begins to experience plastic deformations. These deformations are determined using the previously defined expressions.

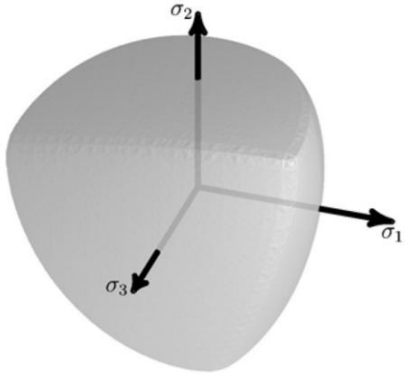

Figure 1. Menetry-Willam yield surface.

The yield surface is defined as:

$$f_{MW} = \frac{c_2}{c_3}\left[\sqrt{\frac{2}{3}}I_1 + r\sqrt{2J_2}\right] + 2J_2 - \frac{1}{c_3} \quad (4)$$

where, I_1 is the first invariant of σ and J_2 is the second invariant of the stress deviatoric tensor *S*. In equation (1), C_2, C_3 and γ depend on material parameters and the hardening and softening functions:

$$c_2 = \frac{1}{\sqrt{6}}\left[\frac{1}{\overline{R_c}} - \frac{1}{\overline{R_b}} + \frac{\overline{R_b}-\overline{R_t}}{\overline{R_c}^2}\right] \quad (5)$$

$$c_3 = \frac{3}{2}\frac{1}{\overline{R_c}^2} \quad (6)$$

$$r = \frac{4\left(1-e^2\right)cos^2\theta+(2e-1)^2}{2(1-e^2)\cos\theta+(2e-1)\sqrt{4(1-e^2)cos^2\theta+5e^2-4e}} \quad (7)$$

$$\overline{R_t} = R_t\Omega_{tc} \quad , \quad \overline{R_c} = R_c\Omega_c \quad , \quad \overline{R_b} = R_b\Omega_c \quad (8)$$

$$\Omega_{tc} = \begin{cases}\Omega_t & \kappa_c \le \kappa_{cm} \\ \Omega_t\Omega_c & \kappa_c > \kappa_{cm}\end{cases} \quad (9)$$

$$\epsilon = \frac{\overline{R_t}}{\overline{R_b}} * \frac{\overline{R_b}^2-\overline{R_c}^2}{\overline{R_c}^2-\overline{R_t}^2}, \quad e = \frac{1+\epsilon}{2-\epsilon} \quad (10)$$

$$\cos 3\theta = \frac{3\sqrt{3}}{2}\frac{J_3}{\sqrt{J_2{}^3}} \quad (11)$$

Where: R_t, R_c and R_b, are the attractive, compressive and biaxial residences, respectively. Ω_t and Ω_c are the hardening and softening functions, respectively, which depend on K_t and K_c which are the tensile and compressive hardening variables, respectively. J_3 is the third invariant of the stress deviator tensor S and K_{cm} is a material parameter which is a threshold in the function Ω_c and will be explained later.

The increment of the hardening variables can be calculated as:

$$\dot{\kappa}_c = \frac{\alpha_c}{\overline{R_t}}\boldsymbol{\sigma} : \dot{\boldsymbol{\varepsilon}}^{\boldsymbol{pl}} \quad (12)$$

$$\dot{\kappa}_t = \frac{\alpha_t}{\overline{R_t}}\boldsymbol{\sigma} : \dot{\boldsymbol{\varepsilon}}^{\boldsymbol{pl}} \quad (13)$$

Where, $\sigma\cdot\varepsilon^{pl}$ denotes the scalar product between the stress tensor and the increment of the plastic strain tensor respectively. α_c and α_t are the compressive and tensile weight functions, respectively, defined as:

$$\alpha_c = 1 - \alpha_t \quad (14)$$

$$\alpha_t = \begin{cases} 0 & \tan\alpha < -2 \\ \frac{1}{1+e^{-10\tan\alpha}} & -2 \le \tan\alpha \le 2 \\ 1 & \tan\alpha > -2 \end{cases} \quad (15)$$

$$\tan\alpha = \frac{I_1}{\sqrt{J_2}} \quad (16)$$

The function of hardening and softening in compression are defined as follows:

$$\Omega_c = \Omega_{ci} + (1 - \Omega_{ci})\sqrt{2\frac{\kappa_c}{\kappa_{cm}} - \frac{{\kappa_c}^2}{{\kappa_{cm}}^2}} \quad \text{(for } k_c < k_{cm}\text{)} \quad (17)$$

$$\Omega_c = 1 - (1 - \Omega_{cu})\left(\frac{K - K_{cm}}{K_{cu} - K_{cm}}\right)^2 \quad \text{(for } k_{cm} < k_c < k_{cu}\text{)} \quad (18)$$

$$\Omega_c = \Omega_{cr} + (\Omega_{cu} - \Omega_{cu})e^{\left(2\frac{\Omega_{cu}-1}{K_{cu}-K_{cm}} * \frac{\kappa_c - K_{cu}}{\Omega_{cu} - \Omega_{cr}}\right)} \quad \text{(for } k_c > k_{cu}\text{)} \quad (19)$$

Where K_{cm} and K_{cu} are material parameters corresponding to the value of the compression hardening variable at the transition of its different branches. In particular, K_{cm} is the value of the compression hardening variable at the peak of the Ω_c function and occurs when $\Omega_c = 1$. Ω_{ci} is the initial value of Ω_c, Ω_{cu} is the value corresponding to K_{cu} and Ω_{cr} is the value when K_c tends to infinity.

The function of hardening and softening in traction is defined as:

$$\Omega_t = e^{-\frac{\kappa_c}{a_t}} \quad (20)$$

$$a_t = \frac{g_{ft}}{R_t} \quad (21)$$

$$g_{ft} = max\left(\frac{G_{ft}}{L_i}, \frac{{R_t}^2}{E}\right) \quad (22)$$

Where g_{ft} is the tensile fracture energy. L_i is the effective length of the element and must be determined so that the following equation is satisfied

$$\int_0^\infty \Omega_t \, d\kappa_t = \frac{g_{ft}}{R_t} \quad (23)$$

The hardening and softening functions in tension and compression can be seen in Fig. 2. These functions can be obtained experimentally by means of uniaxial tensile and compression tests.

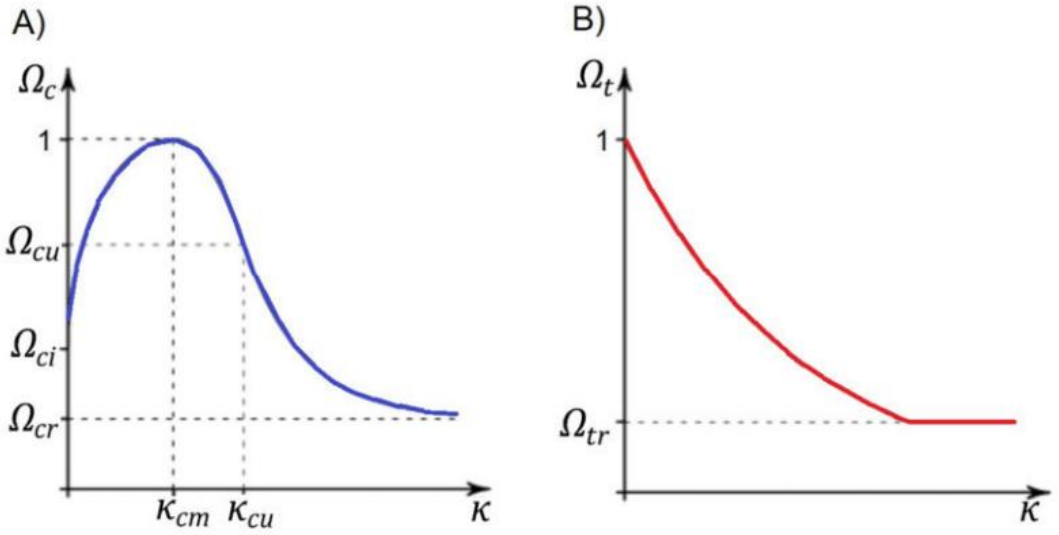

Figure 2. Hardening and softening functions in (A) tension and (B) compression.

The model uses non-associative flow, so the potential function is defined as:

$$Q_{MW} = 2J_2 + B_g\sqrt{2J_2} + C_g\frac{1}{\sqrt{3}}I_1 \quad (24)$$

$$B_g = \frac{2\overline{R_c}\tan\Psi - \sqrt{2}\overline{R_t}}{\sqrt{3}(1-\sqrt{2}\tan\Psi)} \quad (25)$$

$$C_g = \frac{B_g}{\sqrt{2}} + \frac{2\overline{R_t}}{\sqrt{3}} \quad (26)$$

Where Ψ is the dilatancy angle. To summarize, the model has 3 sets of parameters to be defined:

- Elastic Parameters: E and μ.
- Creep Surface Parameters and Potential Function: R_t, R_c, R_b and Ψ.
- Hardening and Softening Function Parameters: k_{cm}, k_{cu}, Ω_{ci}, Ω_{cu}, Ω_{cr}, Ω_{tr} and G_{ft}.

3. Numerical Tests on Notched Beams

Once the model to be used was selected, the parameters of plain concrete and concrete reinforced with 40 kg/m^3 and 80 kg/m^3 of hooked steel fibers (length = 60 mm and diameter = 0.7 mm) were adjusted based on laboratory flexural tests of notched beams. A schematic of the geometry, loading conditions and displacements of the tests performed is shown in Fig. 3.

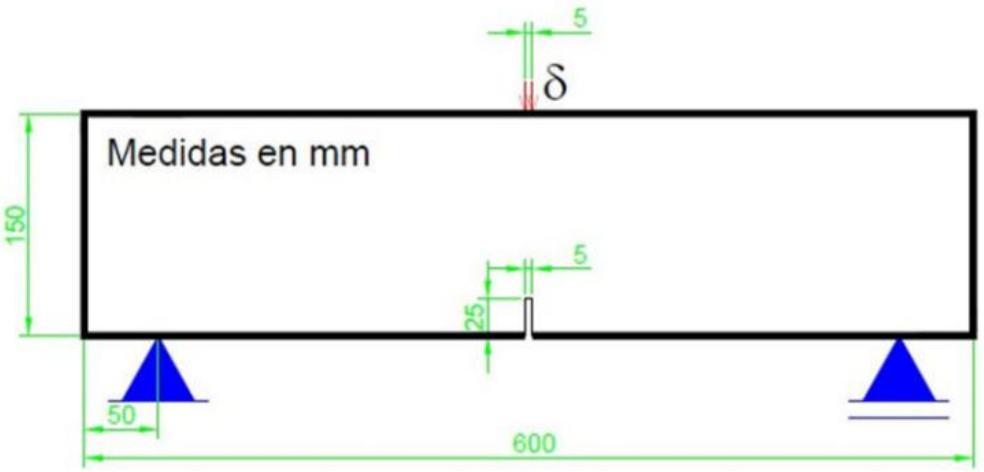

Figure 3. Schematic diagram of notched beam bending tests.

Fig. 4 shows a schematic of the finite element mesh where the central area is framed by a red rectangle. Different mesh refinements were performed in this area (Fig. 5) to test the objectivity of the response with respect to the mesh size.

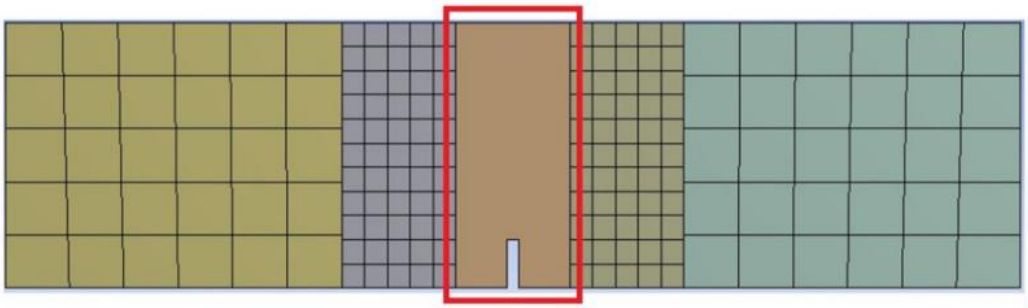

Figure 4. Finite element meshing of notched beams.

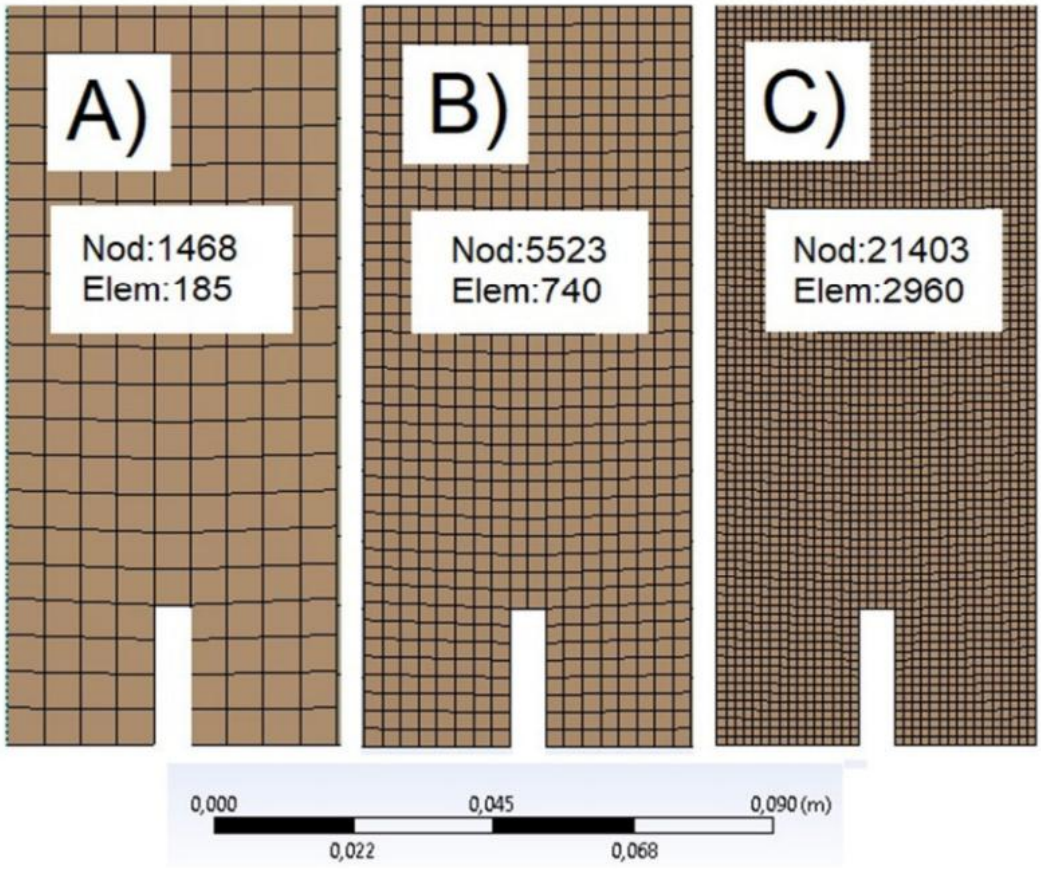

Figure 5. Mesh refinements in the center section of the notched beams.

The load vs. vertical displacement diagrams in the central section obtained numerically for the different finite element meshes can be seen in Fig. 6, where it can be observed that the response is practically independent of the mesh size.

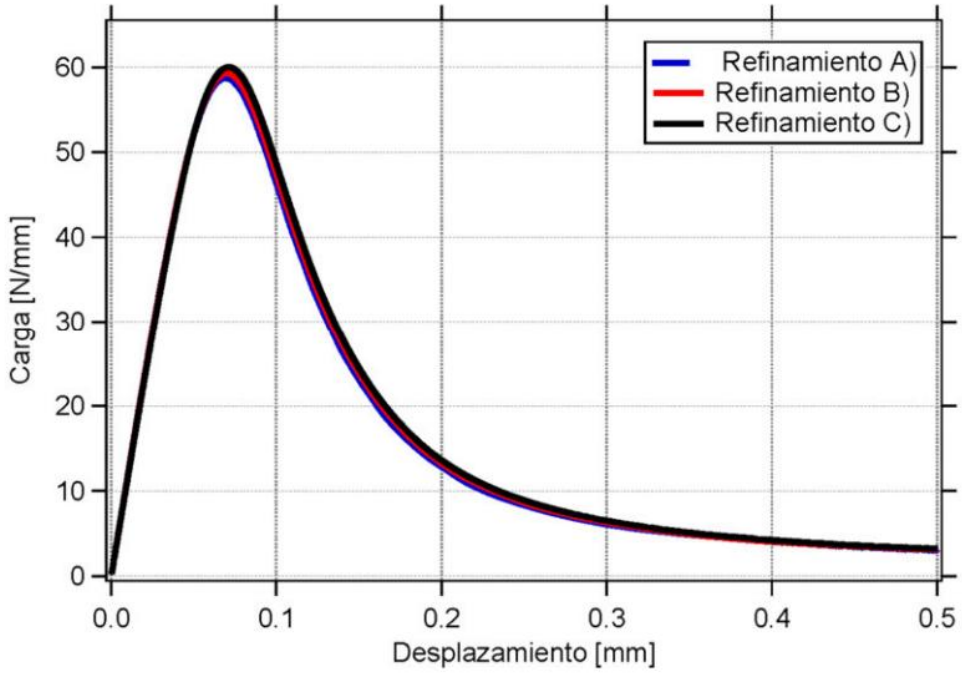

Figure 6. Load-displacement curves. Effect of mesh size.

Then, adopting the mesh of Fig. 5. A, tests were performed varying the fracture energy and tensile strength were performed to analyze the influence of these parameters on the response. The response curves obtained (mean load and vertical displacement) are shown in Figures 7 and 8, respectively. Finally, adjustments were made to the experimental response of slotted beams made of 40 kg/m^3 and 80 kg/m^3 fiber reinforced concrete and ordinary concrete. Figure 9 shows the numerical results and compares them with the experimental results of Load vs. CMOD by Isla et al. (2015) and Luccioni et al. (2017).

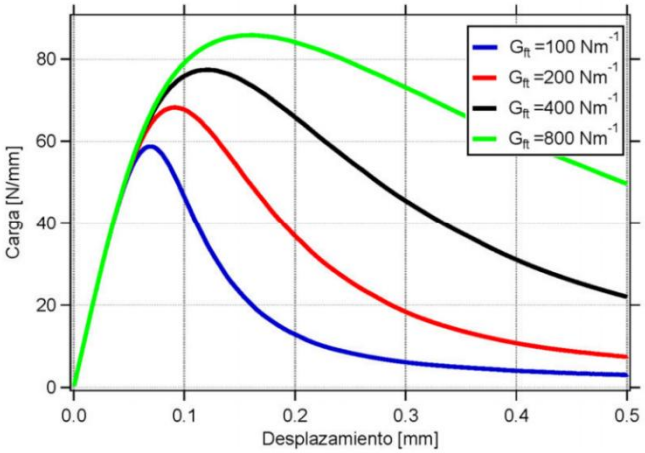

Figure 7. Load-displacement curves. Effect of fracture energy.

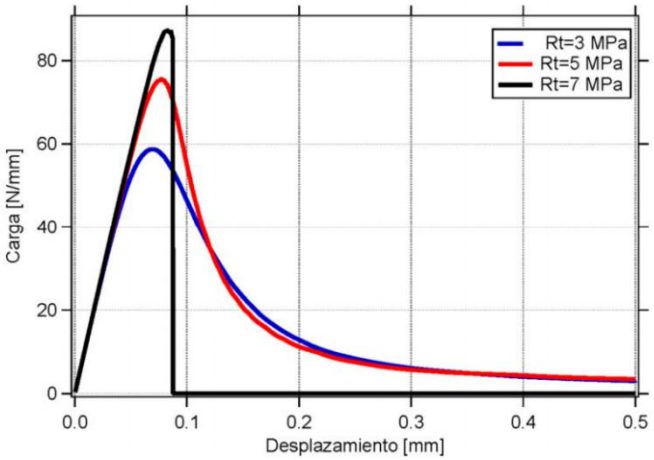

Figure 8. Load-displacement curves. Tensile strength effect.

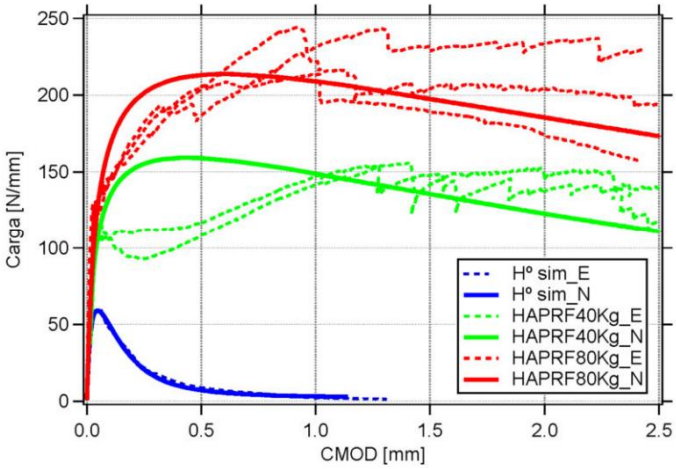

Figure 9. Experimental response adjustment.

Table 1 contains the final parameters obtained to achieve the adjustment.

Table 1. Parameters adjusted in tests

Parameter	H° Sim	HPFRC40	HPFRC80
E (MPa)	27,000	25,000	25,000
μ	0.2		
Rc (MPa)	37	100	100
Rt (MPa)	2.7	4.5	6
Rb (MPa)	45	120	120
Ψ (°)	10		
Kcm	0.001		
Kcu	0.002		
Ωci	0.33		
Ωcu	0.7		
Ωcr	0.05		
Gft (N/M)	200	10,000	20,000
Ωtr	0.05		

Figs. 10 and 11 show the plastic strain and horizontal stress maps for a vertical displacement of the beam center of 0.5 mm from the beam in Fig. 5 A.

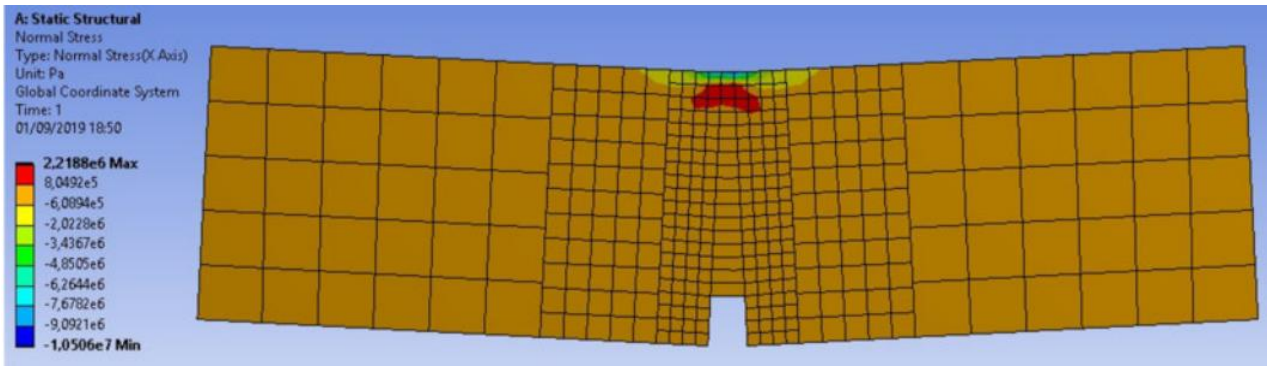

Figure 10. Horizontal stress map for δ = 0.5 mm. Deformation x100.

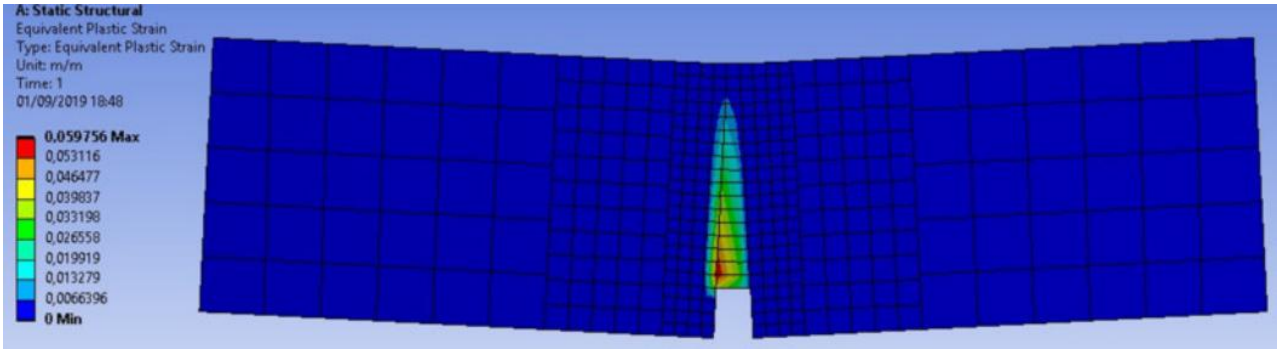

Figure 11. Plastic deformation map for δ = 0.5 mm. Deformation x100.

4. Numerical Tests on Reinforced Concrete Beams

Subsequently, the model was used to numerically reproduce the response of reinforced concrete beams reinforced with HPFRC layers subjected to bending. The geometry, position of loads and supports used, responds to experimental tests performed by Al Osta et al. (2017) which are schematized in Fig. 12 A. Three tests corresponding to the cross sections shown in Fig. 12 B, C and D were numerically simulated.

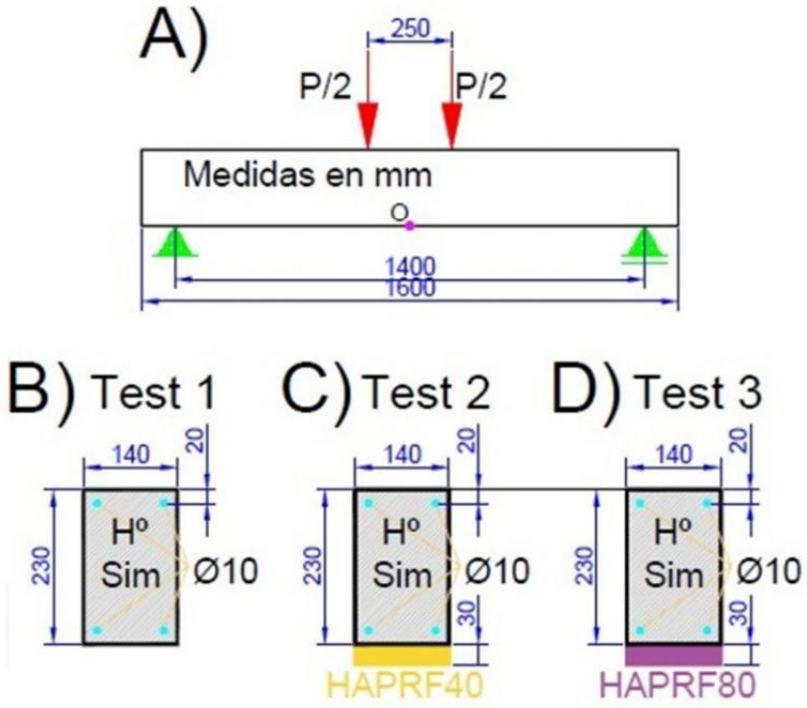

Figure 12. Tests of Hº beams reinforced with HPFRC.

Test 1 corresponds to a reinforced concrete beam. In Tests 2 and 3, two different fiber concrete reinforcements are added to the beam in Test 1. Table 1 shows the material properties of both the beam and the reinforcement.

The steel bars used in all tests were 10 mm in diameter and their mechanical properties were taken according to Al Osta et al. (2017). The Young's modulus and Poisson's ratio of the steel were taken as follows: E = 240,000 MPa and μ = 0.3, respectively. For the steel bars, a bilinear model with a yield point reached at a deformation of 0.3% was considered for the steel bars at a deformation of 0.3% and a stress of 560 MPa.

Figs. 13 and 14 show the finite element mesh of one of the beams with fiber reinforcement and the mesh of the steel bars, respectively. For the concrete, 27-node hexahedral solid elements were used, while 2-node bar elements were used for the steel bars. The contact between concrete and steel was established by matching nodes of both elements such that they had the same displacement. All tests were performed up to a vertical displacement of the load application points of 5 mm. This value was initially set to work with a linear behavior of the steel in the first instance of simulations, meaning that in no case did the deformation exceed 0.3%.

The responses of the simulations are shown in Fig. 15. The numerical results obtained show the same trend as the experimental results found in Al Osta et al. (2017), although a comparison of them was not carried out in this instance of the work. Figs. 16 and 17 show respectively the deformation of the beam and steel bars for a displacement of 5 mm from the load application point in the case of Test 3. Fig. 18 presents the plastic deformation maps of all the Tests for a

displacement of 5 mm from the load application point.

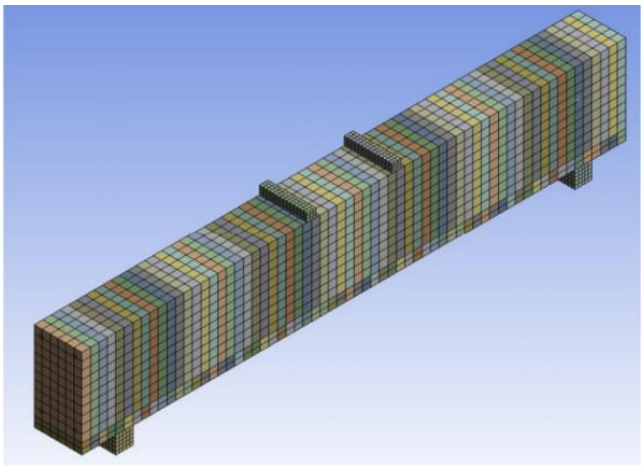

Figure 13. Finite element mesh for beam.

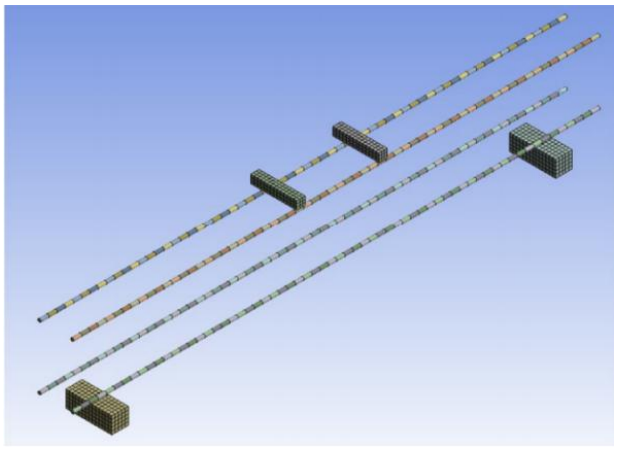

Figure 14. Finite element mesh for members.

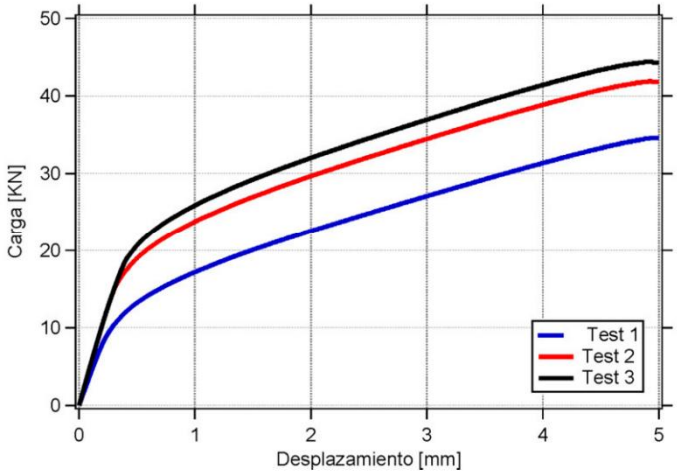

Figure 15. Response of the tests.

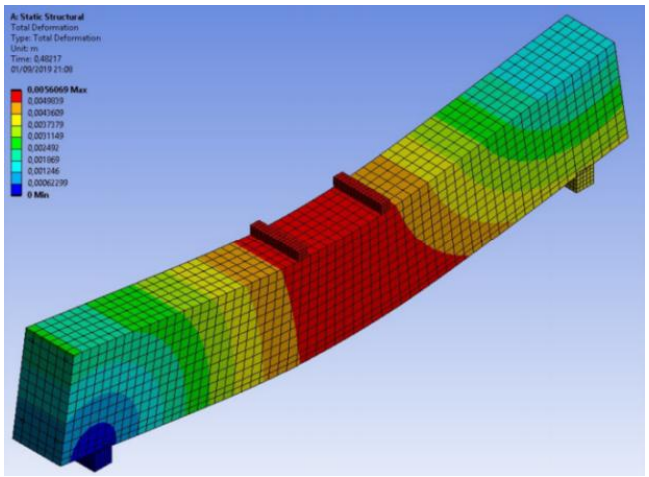

Figure 16. Deformation of Test 3 beam for a displacement of 5 mm. Deformation x50.

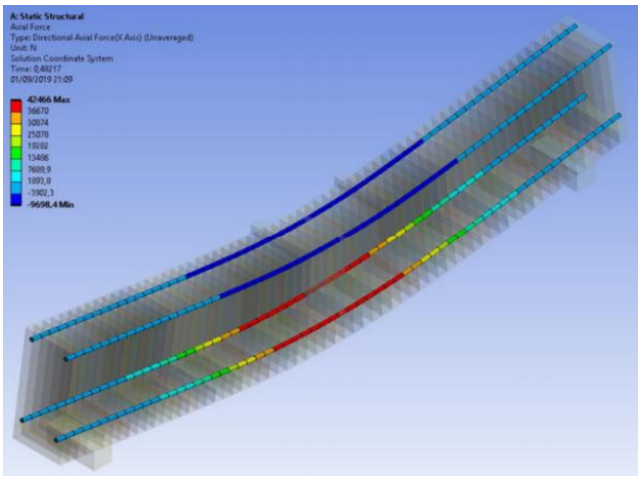

Figure 17. Deformation of the bars of Test 3 for a displacement of 5 mm. Deformation x50.

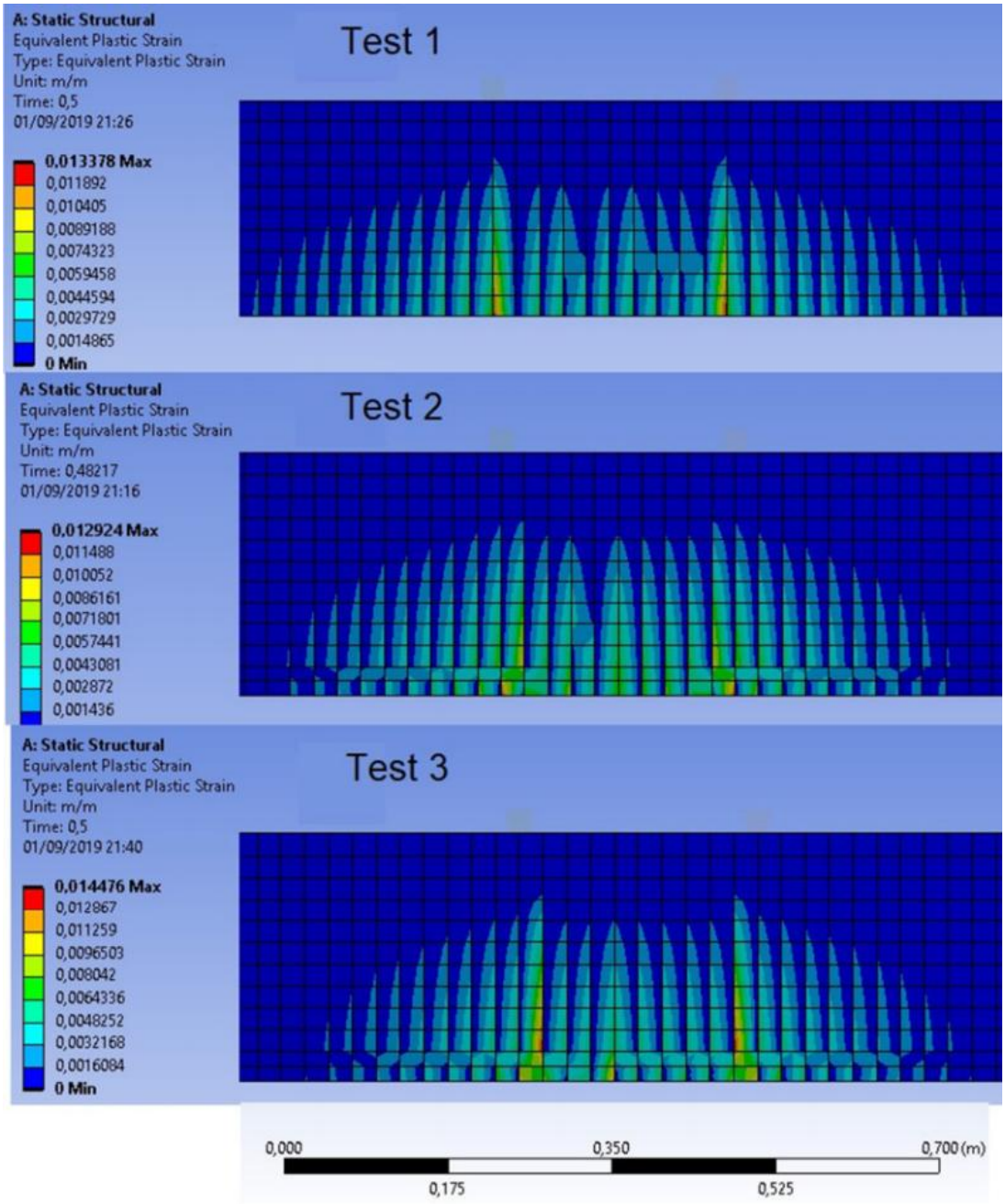

Figure 18. Plastic deformation maps.

5. Conclusions

The results of simulations of HPFRC beams tested under flexural loading show no dependence on the finite element mesh. The model is capable of reproducing the flexural behavior of plain concrete beams and approximating the response of HPFRC beams with 40 and 80 kg/m³ of fibers. Reinforcements made with HPFRC in reinforced concrete beams enhance their flexural strength, and this enhancement is greater the higher the fiber content.

Acknowledgments

The authors of this work are grateful to: Asociación Cooperadora Facet-UNT and Project PICT-2017-1313.

Conflicts of Interest

The author declares no conflicts of interest regarding the publication of this paper.

References

[1] Nanni A. 2012. A new tool for concrete and masonry repair. *Concrete International*, 34: 9-43.

[2] Tysmans T., Wozniak M., Remy O., Vantomme J. 2015. Finite element modelling of the biaxial behaviour of high-performance fibre reinforced cement composites (HPFRC) using concrete damaged plasticity. *Finite Elements in Analysis and Design*, 100: 47-53.

[3] Yu R., Spiesz P., Brouwers H. 2015. Development of ultra-high performance fibre reinforced concrete (UHPFRC): Towards an efficient utilization of binders and fibres. *Construction and Building Materials*, 79: 273-282.

[4] Menetrey P. Willam K. 1995. Triaxial failure criterion for concrete and its generalization. *ACI Structural Journal*, 92: 311-318.

[5] Isla F., Luccioni B., Ruano G., Torrijos M., Morea F., Giaccio G., Zerbino R. 2015. Mechanical response of fiber reinforced concrete overlays over asphalt concrete substrate: experimental results and numerical simulation. *Construction and Building Materials*, 93:1022-1033.

[6] Luccioni B., Isla F., Codina R., Ambrosini D., Zerbino R., Giaccio G., Torrijos M. 2017. Effect of steel fibers on static and blast response of high strength concrete. *International Journal of Impact Engineering*, 107: 23-37.

[7] Al-Osta M., Isa M., Baluch M., Rahman M. 2017. Flexural behavior of reinforced concrete beams strengthened with ultra-high performance fiber reinforced concrete. *Construction and Building Materials*, 134: 279-296.